

Instrumentation for Real-Time Dynamic Optical Tomography

Christoph H. Schmitz^{*a}, Yaling Pei^b, Harry L. Graber^a, Joseph M. Lasker^{a,c},
Andreas H. Hielscher^{a,c}, and Randall L. Barbour^{a,c}

^aDept. of Pathology, SUNY Downstate Medical Center, Brooklyn, NY 11203, U.S.A.

^bNIRx Medical Technologies Corp., Glen Head, NY 11545, U.S.A.

^cDept. of Electrical and Computer Engineering, Polytechnic University,
Brooklyn, NY 11201, U.S.A.

ABSTRACT

Presented are the operating characteristics of an integrated CW-near infrared tomographic imaging system capable of fast data collection and producing 2D/3D images of optical contrast features that exhibit dynamic behavior in tissue and other highly scattering media in real time. Results of preliminary *in vivo* studies on healthy and cancerous breast tissue are shown.

Keywords: Dynamic imaging, optical tomography, mammography, instrumentation

1. INTRODUCTION

Recently, we have put forward the idea that dynamic optical tomography can be used as a general tool for imaging the dynamics of vascular reactivity and tissue oxygen supply/demand as revealed by variations in hemoglobin states for large tissue structures.^{1,2,3} This hypothesis is supported by the observation that rhythmic fluctuations in vessel diameter, due to cardiac, respiratory or vasomotor activity, produces local changes in tissue hemoglobin levels that in turn influence the intensity of transmitted light. In addition, by performing a multi-wavelength measurement, local fluctuations in the oxygenation state of hemoglobin can be simultaneously assessed. This capability, when combined with the collection of a continuous time series of imaging data, allows for the *in situ* exploration of the spatiotemporal dynamics of vascular reactivity and hemoglobin states. Because these are linked to numerous basic physiological processes and tissue pathologies, we believe that the full development of this capability could prove of fundamental importance for the detection and management of a broad range of clinical conditions including peripheral vascular disease, tumor detection and its response to therapy, and functional brain studies.

In a series of recent reports we have described the basic instrumentation,^{4,5,6} image reconstruction methods,^{7,8} and approaches to image analysis^{9,10} that allow for the extraction and spatial mapping of the relevant functional measures associated with these states. In the current report we present a description of an integrated hardware and software approach that provides for the real-time imaging of dynamic processes. We also present results from preliminary studies on a subject with breast cancer, to determine whether we can detect a state of altered vascular dynamics associated with tumor angiogenesis. We have considered this case because of the abundant evidence that tumor-induced angiogenesis, unlike that in the surrounding normal tissue, produces a state wherein the vessels have significant morphological and functional anomalies. These are characterized by vessels that are typically elongated, tortuous, leaky, have dead ends, and mainly lack innervation, thus rendering them poorly controlled by autonomic stimuli.¹¹ Results obtained show a notably more spatially incoherent temporal response of the vasculature following a respiratory challenge, compared to the contralateral tumor-free breast.

* cschmitz@downstate.edu; Phone: (718) 270-2832; Fax: (718) 270-3313; <http://138.5.51.241/index/>; SUNY Downstate Medical Center, Dept. of Pathology, Box 25, 450 Clarkson Ave., Brooklyn, NY 11203, USA

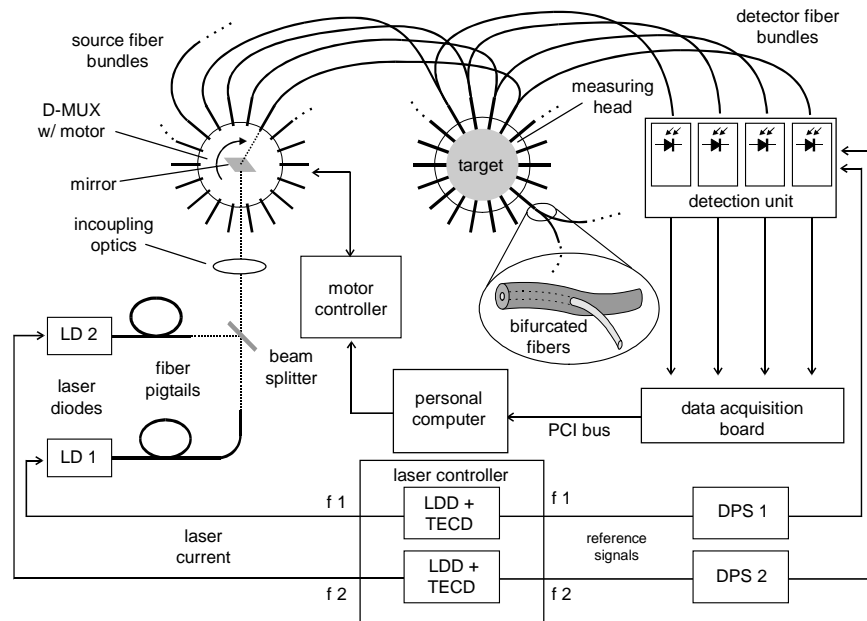


Fig. 1: Block Diagram of the optical imager. LD: laser diodes, LDD: laser diode driver, TECD: thermo-electric cooler driver, f1,2: laser modulation frequencies, DPS: digital phase shifter, D-MUX: optical demultiplexer..

2. METHODS

2.1. Instrumentation

As discussed in previous reports,⁴⁻⁶ a host of design parameters should be considered when realizing a setup capable of full tomographic optical imaging of thick tissue structures at a fast framing rate. The details of this depend on the intended application, and include various particulars associated with data collection and required data analysis times (*i.e.*, real time or offline). Fig. 1 shows the block diagram of the instrument developed by the Optical Tomography Group at SUNY Downstate Medical Center.

The beams of two or more laser diodes operating in the 800 nm range are collinearly overlaid and coupled into one of multiple source fiber bundles. Fast switching between different sources is possible by means of an optical demultiplexer (D-MUX), which consists of a mirror rotated by a microprocessor-controlled brushless DC servomotor that allows for fast precise positioning. It is essential that the mirror completely stop for a short time (~ 10 ms) in order to minimize degradation of system precision due to variations in light intensity during the detection process. The motor chosen and its microprocessor-equipped motion control unit allow very flexible implementation of customized motion protocols. The unit is capable of performing ~ 75 start-stop motions per second without noticeable overshooting or ringing. The motor controller acts as the main clock for timing the various tasks such as advancing the source positions, performing the light detection, and acquiring/storing the data.^{5,6} Each source fiber bundle (1 mm dia.) forms one branch of a bifurcated fiber bundle and joins the other branch (3 mm dia.), which is used for light detection, in a bull's-eye geometry on the target surface. Each detector fiber bundle terminates at one silicon photodiode of a multi-channel detection module. As many as 32 detector channels are housed by one compact 19" unit. Each of the channels incorporates: analog signal conditioning hardware, such as adjustable gain stages, to increase the dynamic range of detection; up to four lock-in amplifiers; and sample-and-hold circuits in order to improve signal quality and for timing purposes. The output voltages of the detector channels are measured by a data acquisition board and stored on a personal computer. For purposes of lock-in detection, the laser diodes are current-modulated in the 5-10 kHz range, and digital phase shifters are used to optimize the phase angle between the measured signal and the reference. The mean optical output power of the laser diodes is in the range of 100 mW; the optical power sent to the target is about 30 mW.

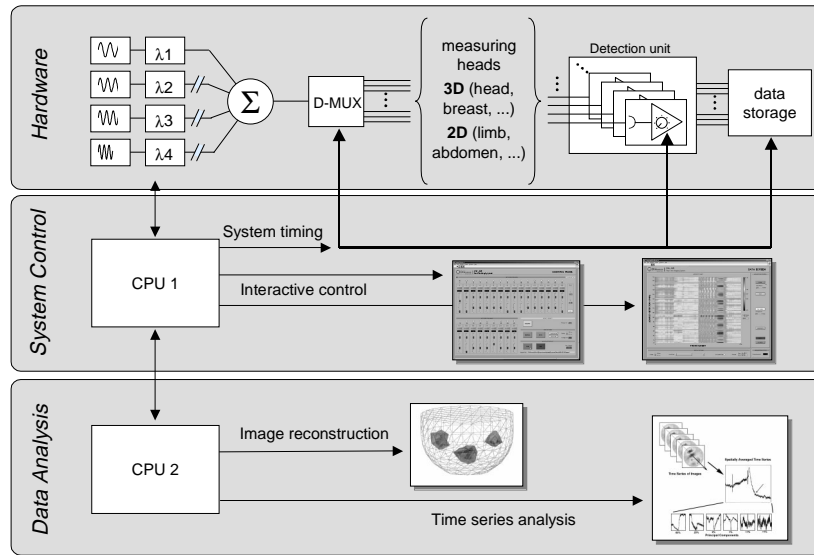


Fig. 2: Schematic of functionality and system architecture. λ_1 -4: lasers of different wavelengths, Σ : Overlaying beams, D-MUX: optical demultiplexer.

2.2. Functionality

The described system employs an architecture that comprises seven levels of hardware/software functionality. A schematic representation of this is depicted in Fig. 2.

The hardware level features use of frequency-encoded multiwavelength DC illumination, a time-multiplexed source, and parallel multi-channel detection, together with on-the-fly fast gain switching (dynamic range of 180 dB). Fully configured, the basic unit can provide four wavelengths of simultaneous illumination at each illuminating site and can collect data from 32 channels at a source switching rate of ~ 75 Hz. This provides a data acquisition rate of between ~ 2.2 and ~ 8.8 kHz.

System operation is achieved through two levels of software control. The first level is transparent to the operator and is responsible for system timing and data storage. The second level serves as a user interface that is generated within a LabVIEW environment. This level comprises all elements of hardware control, as well as automated setup and alignment procedures.

The collected data are made available to four additional levels of data processing to provide for data viewing and analysis in real time. The first level, also provided by the first CPU and under the LabVIEW environment as well, serves a viewing screen that displays the measured intensity data for all (selected) source-detector pairs in real time.

The second CPU, operating under a Unix environment, provides additional levels of data processing associated with image reconstruction, image display and image analysis. A variety of coupled forward-inverse reconstruction algorithms is available. These allow for image recovery using first-order or recursive finite element based schemes for 2D or 3D problems. All are derived from the diffusion equation for DC illumination. Computed parameters include absorption only, scattering (diffusion) only, or both. Real-time image recovery in the case of first order solutions is derived from schemes recently described.^{7,8}

Computed images are currently displayed within a MATLAB environment. These are presented as a time series of 2D images or, in the case of 3D imaging, as a set of 2D image slices corresponding to each image frame. The latter

format represents a restriction of our currently available display capability and is not related to any restriction stemming from image reconstruction. The computed image series is available for off line interrogation using a spectrum of analysis routines embedded within an interactive MATLAB environment. These allow for the computation and display of linear and nonlinear properties associated with the time-varying pixel data.

Fig. 3 shows a screenshot of the virtual control panel of the imager that we implemented using LabVIEW. The functionality provided includes correction for detector offset (1) and automated or manual (2) gain adjustment of the individual detector channels with respect to the different source locations. In the manual mode, a specific source location can be selected (3), and virtual sliders (4) are used for controlling the gain setting of the detector channels. An automated function is available that repeats this procedure for every source-detector-combination for the purpose of increasing setup speed and reliability. Numerical displays report the signal level for each channel (5). Other functionalities include specification of illuminating wavelengths (6), adjustment of the digital phase shifters (7), selection of the source illumination scheme (single-site or tomographic illumination, 8), number of image frames (9), and data path.

Fig. 4 shows a screenshot of the display screen that appears when initiating a measurement on the control panel. The measured data are presented in a map that shows the color-coded light intensity levels for each source-detector combination. When all available measuring channels are employed, data corresponding to 1024 channels are simultaneously displayed for the selected wavelength. The map scrolls along the time axis as the measurement pro-

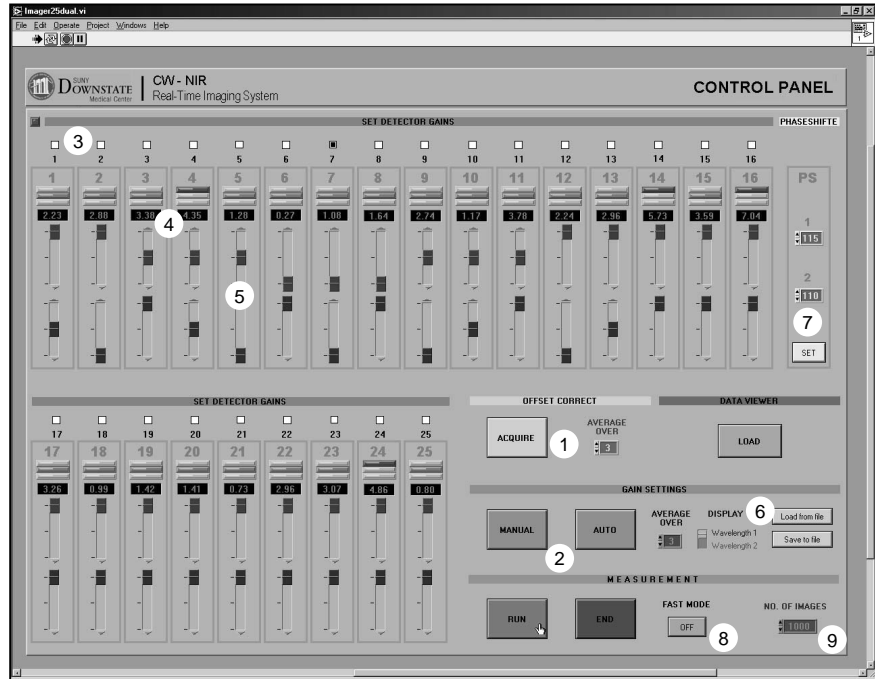


Fig. 3: Virtual control panel. 1: offset correction. 2: manual and automated setup. 3: source selector. 4: detector reading/level indicator. 5: slider for detector gain. 6: wavelength selector. 7: phase shifter control. 8: single-source mode. 9: number of time points to acquire.

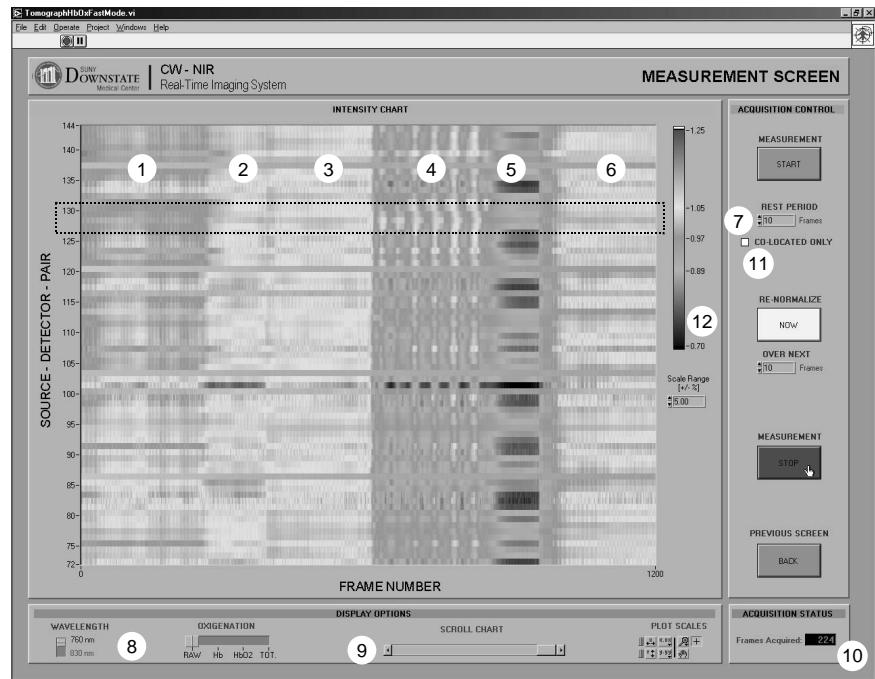


Fig. 4: Real-time data display. 1-6: readings corresponding to various maneuvers (see Fig. 5). 7: length of baseline. 8: display options. 9: data scroll bar. 10: frame count. 11: display co-located source-detectors pairs only. 12: adjust color bar.

ceeds. Shown in Fig. 4 is a plot for an actual measurement. The onset of 6 different volunteer maneuvers – as indicated by numbers 1-6 (1 = rest, 2 = cold pressor test, 3 = recovery, 4 = deep breathing, 5 = breath hold, 6 = recovery) – can clearly be distinguished. This kind of feedback provides a very useful tool when developing provocation protocols. Data shown are the relative changes in the readings for each source-detector combination with respect to an initial baseline period whose length can be chosen (7). The display screen provides for different display options (8). This includes the display of the raw data at either wavelength or of the computed changes in hemoglobin states (oxy, deoxy, total). Various other functionalities are implemented, such as a data scroll bar (9), display of the actual count of frames acquired (10), optional display of the readings for the co-located source-detector pairs only (11), and interactive adjustments of the display’s axes and color scale ranges (12).

3. RESULTS

In this section, we present some preliminary clinical results obtained with the real-time imaging system described above. Measurements were performed on both a healthy volunteer and one with a large infiltrating ductal carcinoma.

3.1. Healthy Volunteer

Fig. 5 shows five exemplary detector readings obtained from a 6-min. measurement on the breast of a healthy volunteer. The traces were normalized to their respective mean value during the initial rest period (225 time points) and offsets of incremental multiples of 0.2 have been introduced for display purposes. Measurements were made by having the patient lie prone with one breast hanging pendant through a 7"-diameter opening. A folding hemisphere structure, described earlier,⁴ was used to create optical contact between the tissue and the optical source and detector fibers, to conform the breast to a hemispherical shape, and to provide stabilization against motion artifacts. The data shown were obtained at 810 nm, which is near the isobestic point of hemoglobin, and thereby represent changes in blood volume. Indicated are six different phases of the experiment according to different maneuvers performed by the volunteer listed in Fig. 4. During phases 1-3 and 6, a normal respiratory frequency is prominent. A change to larger amplitude and lower frequency occurs during deep breathing (phase 4). Phase 2 shows the response of the breast vasculature to a cold pressor test ad-

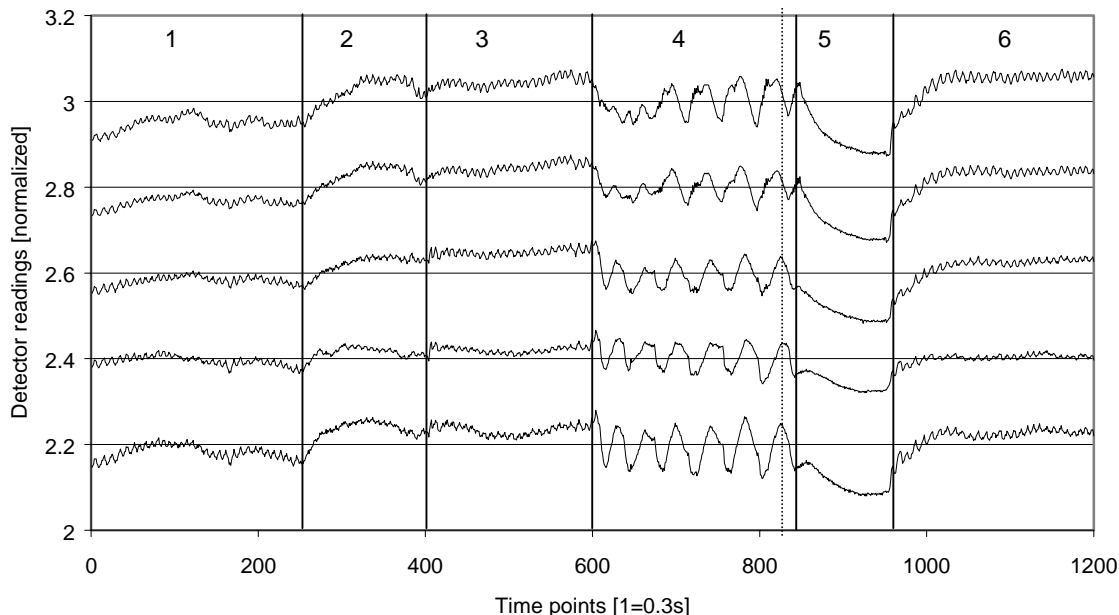


Fig. 5: Five representative detector readings from a breast measurement on a healthy volunteer. Readings are normalized and shifted. The encircled numbers refer to various maneuvers (1 = rest, 2 = cold shock, 3 = recovery, 4 = deep breathing, 5 = breath hold, 6 = recovery). The traces shown correspond to the area in Fig. 4 indicated by a dashed line.

ministered to the subject’s contralateral hand. Observed is an increase in the intensity of transmitted light, a finding consistent with the known vasoconstrictive response to a cold shock. Period 5 shows an absence of the respiratory frequency, which is the expected response to a breath hold.

Careful inspection of the detector data reveals that despite their qualitative similarity, notable differences are present. For instance, during deep breathing, we see that the phase of the respiratory signal can differ. This is indicated by the vertical dotted line in Fig. 5. This finding suggests that localized time lags in venous return occur, perhaps in response to intrinsic differences in venous return, or to small differences in contact pressure exerted by the measuring head, *etc.* The point is that the details in the vascular response most certainly can depend on differences in tissue composition, differential external pressure, local differences in metabolic needs, *etc.* By performing a continuous multi-site tomographic measurement, we have the ability to detect and image these variations.

3.2. Patient Measurements

The large amount of data that can be collected using the described instrument argues for the need to explore more global measures before considering possible detailed differences between healthy and diseased tissue. One such measure is the spatially integrated time-varying signal. This is represented by the mean value of the normalized time course over all source-detector pairs. Fig. 6 shows the integrated response determined for the tumor free breast (9 cm dia.) obtained from a 17 source \times 17 detector measurement (289 source-detector pairs). The normalization was performed by computing the temporal mean value for the first 30 time points (not shown) for each source-detector pair and expressing all subsequent values relative to this. Thus each source-detector pair is normalized to itself. The absolute intensity readings for this measurement varied over a range of 10^7 . Indicated are 4 phases of a provocation protocol: 1) rest period, 2) deep breathing, 3) breath hold, 4) recovery.

Inspection reveals that the integrated signal exhibits considerable spatial coherence throughout the entire time course. The dominant frequency observed is due to respiration, which is greatly amplified by deep breathing and absent during a breath hold. This finding is consistent with the known modulation of venous return caused by respiration.¹² We wish to emphasize that, contrary to what some have suggested, these findings are almost certainly not attributable to any respiration-induced instability in optode-tissue contact. This is supported by repeated careful observations that firm contact is made between the breast and all measuring sites upon closure of the folding hemisphere. In addition, similar observations made simultaneously on opposing sides of the breast during the deep breathing activity failed to reveal any modulation in tissue contact.

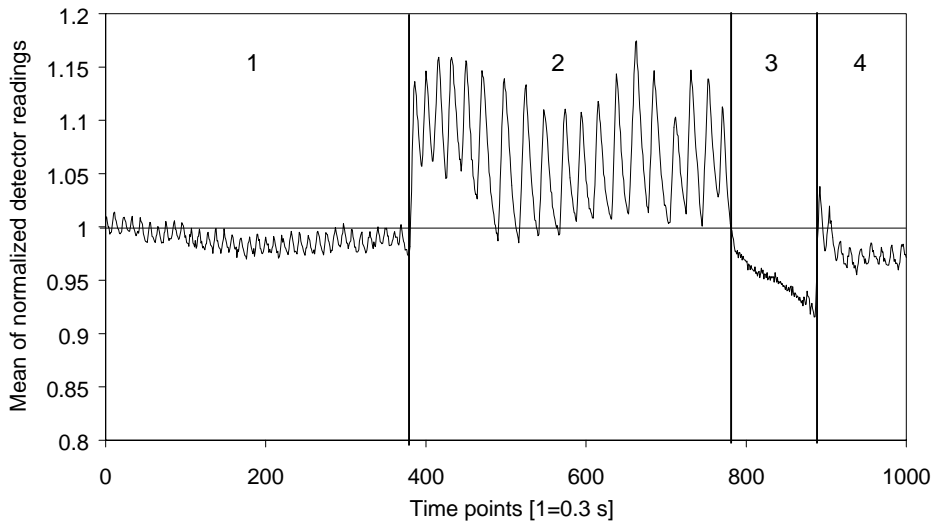


Fig. 6: Plot of the time varying mean value for all normalized detector readings, healthy breast.

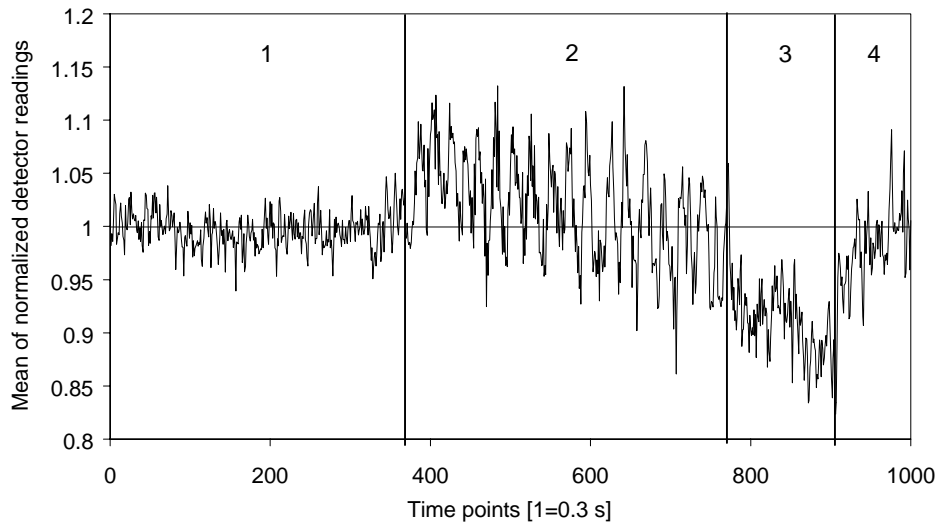


Fig. 7: Plot of the time varying mean value for all normalized detector readings, tumor bearing breast.

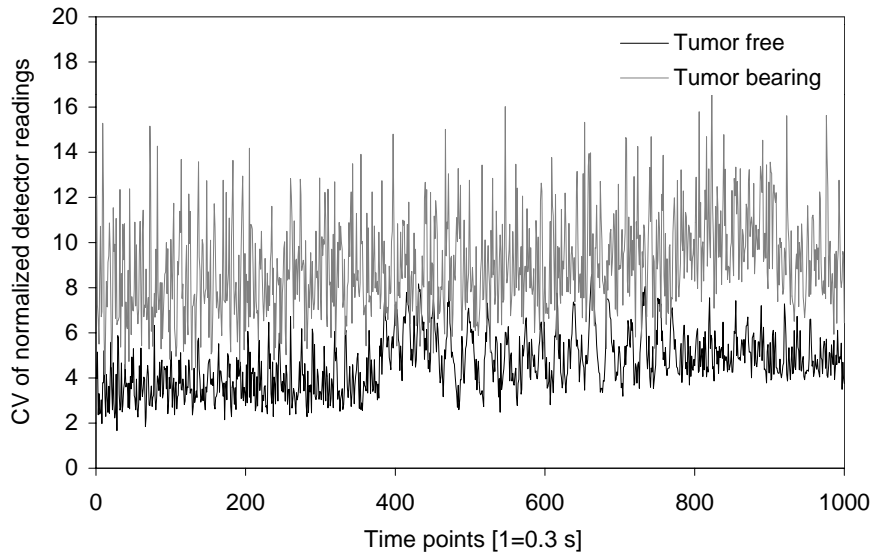


Fig. 8: Plot of the time varying C.V. values for all normalized detector readings, both breasts.

The corresponding result for the tumor-bearing breast is shown in Fig. 7. Here we see a markedly less coherent response that cannot be attributed to only differences in signal amplitudes. While it is the case that the tumor-bearing breast was slightly larger in diameter (~10 cm), the signal quality for all but the most distant detectors was comparable to that obtained in the previous case. We interpret the added temporal variability of the integrated signal as suggestive of a more disorganized vascular response, both for baseline vascular activity and in response to provocation. Evidence in support of this interpretation is provided in Figure 8.

Here we have computed the coefficient of variation (CV) at each time point for the integrated signal. Increased variance means that the normalized detector values are more dissimilar, indicating that some regions of tissue are experiencing greater variations in hemoglobin levels than others. Inspection of the time series during the rest period for the

tumor-free breast fails to reveal any overt beat frequency (confirmed by FT, not shown). In contrast, upon deep breathing we observe a distinct beat frequency that coincides with the rate of deep breathing. Note that this does not simply indicate that the tissue blood volume varies with the respiratory frequency, which it certainly does, but rather that the degree to which it varies is not spatially uniform, or constant in time. We interpret this finding to simply reinforce the general notion that blood perfusion in tissue is both spatially and temporally heterogeneous. The more significant observation is that seen in the tumor-bearing breast. Here we see no evidence of a similar phenomenon upon deep breathing. To eliminate the possibility that this is simply due to the influence of more noisy detector readings, we eliminated those detectors having the lowest signal levels (detectors located $> \pm 135^\circ$ from any source) from the calculation, which is the time course shown. Thus, we are left with the suggestion that the normal spatiotemporal organization of the vascular response in the tumor-bearing breast is distinctly different from that of the tumor-free breast, a finding consistent with our indicated hypothesis.

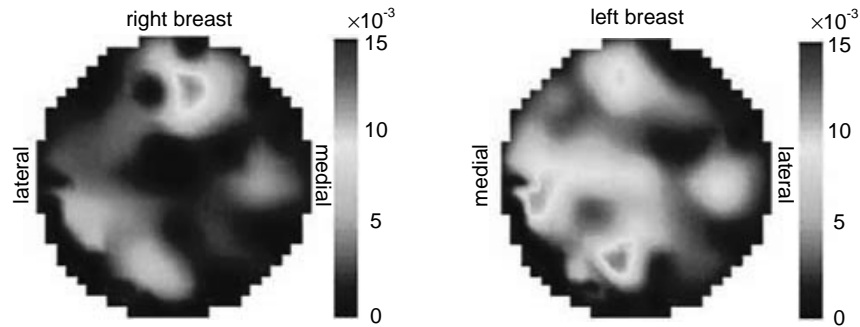


Fig. 9: Coronal view of the reconstructed amplitude map for the respiratory frequency.

Of added interest are efforts to generate functional image maps of the breast that reveal the location of temporal features observed in the detector data. While many such features can be considered, here we have generated maps that reveal the vascular response to deep breathing which is known to modulate venous return. This was computed by first obtaining the Fourier coefficients of the time series for all source-detectors pairs and computing from this a spatial map corresponding to the amplitude at the deep breathing frequency. Fig. 9 shows a coronal view of reconstructed functional images for both breasts taken midway between the chest wall and the nipple. The color scale reveals the amplitude the observed response. Comparison shows that a significantly reduced amplitude is seen along the line between 4:30-10:30 for the tumor-bearing right breast compared to its conjugate orientation along the line between 1:30 and 7:30 in the tumor-free left breast. Significantly, this differential response coincides well with x-ray mammography results (shown in Fig. 10 in a cranio-caudal view) demonstrating the location of the tumor to range from the upper lateral quadrant to the lower medial quadrant, a finding mainly consistent with the indicated region where the attenuated respiratory response is seen (*i.e.*, 7:30-10:30) in the tumor-bearing breast.

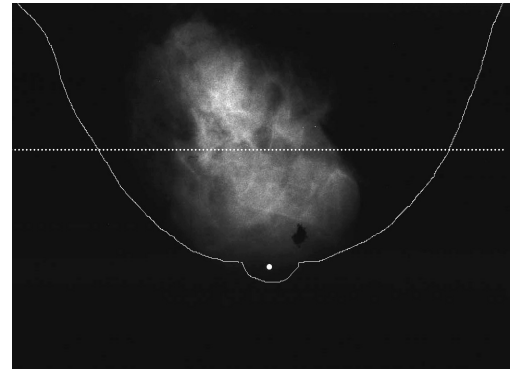


Figure 10: X-ray mammogram of the right (tumor-bearing) breast with indicated boundary (cranio-caudal view). The dashed line shows the approximate position of the coronal sections for the reconstructed optical images.

4. DISCUSSION

In this report we have described an integrated system that is intended to serve as a general-purpose optical imaging platform for the investigation of time-varying hemoglobin states and vascular reactivity in large tissue structures. Expected application areas include use in the investigation of peripheral vascular diseases, functional brain imaging, tumor detection and its response to therapy, among others.

Different instrument configurations have been devised, including a portable cart-based system⁵ to which a variety of measuring heads can be attached, and which contains all the needed electronics and optical devices, CPU's and displays. For mammography applications, we developed a dedicated breast imager, which comprises a gantry on which the patient lies prone with the breast under investigation hanging pendant through an opening. This configuration uses a folding hemispherical structure to create reliable optical contact between the tissue and the optodes and to stabilize the target.

The described optical imaging system comprises seven levels of hardware and software functionality that make the communication between the various system components transparent to the operator and provide an interface with intuitive control and display capabilities. These include the real-time display of the intensity values for different wavelengths and computed changes in hemoglobin oxygenation states. This capability is particularly valuable when establishing provocation maneuvers. In addition, we have implemented the capability of real-time 2D and 3D image reconstruction and display.

Presented are results of a time-series imaging study performed on a tumor-bearing and tumor-free breast of a subject diagnosed with a large ductal carcinoma. Analysis of the time series provides evidence that unlike the coherent response of the tumor-free breast, the temporal dynamics of the tumor-bearing breast is largely incoherent. This finding supports the hypothesis that tumor induced angiogenesis leads to observable disturbances in the temporal dynamics of the vascular response.

5. ACKNOWLEDGEMENTS

This research was supported by NIH grants RO1-CA 66184 (RLB), R01 AR46255-01 (AHH), and the NYC Council Speaker's Fund for Biomedical Research: Towards the Science of Patient Care (AHH).

REFERENCES

- ¹ R. L. Barbour, H. L. Graber, C. H. Schmitz, Y. Pei, S. Zhong, S.-L. S. Barbour, S. B. Blattman, and T. F. Panetta, "Spatio-Temporal Imaging of Vascular Reactivity by Optical Tomography," in Proceedings of Inter-Institute Workshop on in Vivo Optical Imaging at the NIH, A. H. Gandjbakhche, ed. (Optical Society of America, Washington, DC), 161-166 (1999).
- ² R. L. Barbour, H. L. Graber, Y. Pei, S. Zhong, C. H. Schmitz, "Optical tomographic imaging of dynamic features of dense-scattering media," *J. Opt. Soc. Am. A*, in press (2001).
- ³ H. L. Graber, C. H. Schmitz, Y. Pei, S. Zhong, S.-L. S. Barbour, S. Blattman, T. Panetta, R. L. Barbour, "Spatio-temporal imaging of vascular reactivity," in Physiology and Function from Multidimensional Imaging (Proceedings of SPIE **3978**), A. V. Clough, C.-T. Chen, eds., pp. 32-43 (2000).
- ⁴ C. H. Schmitz, H. L. Graber, H. Luo, I. Arif, J. Ira, Y. Pei, A. Bluestone, S. Zhong, R. Andronica, I. Soller, N. Ramirez, S.-L. S. Barbour, and R. L. Barbour, "Instrumentation and calibration protocol for imaging dynamic features in dense-scattering media by optical tomography," *Appl. Opt.*, **39**, 6466-6485 (2000).
- ⁵ C. H. Schmitz, M. Löcker, J. Lasker, A. H. Hielscher, R. L. Barbour, "Performance characteristics of a silicon diode (SiPD) based instrument for fast functional optical tomography," in Optical Tomography and Spectroscopy of Tissue IV (Proceedings of SPIE **4250**), B. Chance, R. R. Alfano, B. J. Tromberg, M. Tamura, E. M. Sevick-Muraca, Eds., pp. 171-179 (2001).
- ⁶ C. H. Schmitz, M. Löcker, J. M. Lasker, A. H. Hielscher, and R. L. Barbour, "Instrumentation for fast functional optical tomography," *Rev. Sci. Instr.*, currently under review (2001).
- ⁷ Y. Pei, H. L. Graber and R. L. Barbour, "Influence of systematic errors in reference states on image quality and on stability of derived information for DC optical imaging," *Appl. Opt.*, 2001, in press.
- ⁸ Y. Pei, H. L. Graber, and R. L. Barbour, "Normalized-constraint algorithm for minimizing inter-parameter crosstalk in DC optical tomography," *Opt. Expr.* **9**, 97-109 (2001).
- ⁹ G. S. Landis, T. F. Panetta, S. B. Blattman, H. L. Graber, Y. Pei, C. H. Schmitz, R. L. Barbour, "Clinical applications of dynamic optical tomography in vascular disease," in Optical Tomography and Spectroscopy of Tissue IV (Proceedings of SPIE **4250**), B. Chance, R. R. Alfano, B. J. Tromberg, M. Tamura, E. M. Sevick-Muraca, eds., 130-141 (2001).

¹⁰ R. L. Barbour, H. L. Graber, Y. Pei, C. H. Schmitz, "Imaging of vascular chaos," in *Optical Tomography and Spectroscopy of Tissue IV (Proceedings of SPIE 4250)*, B. Chance, R. R. Alfano, B. J. Tromberg, M. Tamura, E. M. Sevick-Muraca, eds., 577–590 (2001).

¹¹ M. A. Konerding, C. van Ackern, E. Fait, F. Steinberg, and C. Streffer, "Morphological Aspects of Tumor Angiogenesis and Microcirculation," in: *Blood Perfusion and Microenvironment of Human Tumors: Implications for Clinical Radiooncology*, M. Molls, P. Vaupel, eds. (Springer-Verlag Berlin Heidelberg, 1998), 5-17.

¹² J. Ross, Jr., "Structure–Function Relations in the Peripheral Circulation," Chap. 6 in *Best and Taylor's Physiological Basis of Medical Practice*, 11 th Ed., J. B. West, ed., Williams & Wilkins, Baltimore (1985).